Document downloaded from:

http://hdl.handle.net/10251/197515

This paper must be cited as:

Payri, R.; Gimeno, J.; Marti-Aldaravi, P.; Martínez, M. (2022). Transient nozzle flow analysis and near field characterization of gasoline direct fuel injector using Large Eddy Simulation. International Journal of Multiphase Flow. 148:1-16. https://doi.org/10.1016/j.ijmultiphaseflow.2021.103920

The final publication is available at

https://doi.org/10.1016/j.ijmultiphaseflow.2021.103920

Copyright Elsevier

Additional Information

Payri et al. "Transient nozzle flow analysis and near field characterization of gasoline direct fuel injector using Large Eddy Simulation," Int. J. Multiph. Flow, vol. 148, no. December 2021, p. 103920, 2021. DOI: 10.1016/j.ijmultiphaseflow.2021.103920

Transient nozzle flow analysis and near field characterization of gasoline direct fuel injector using Large Eddy Simulation

Raúl Payri[a], Jaime Gimeno[a], Pedro Martí-Aldaraví[a], María Martínez[a]

[a] *CMT-Motores Térmicos, Universitat Politècnica de València*

Abstract

Injection duration in spark ignition engines is typically very short. Thus, understanding transient effects of the Gasoline Direct injection (GDi) process plays a major role in the analysis of the mixture formation and so combustion efficiency in this type of engines. Focusing on the opening and closing phases when the needle is moving up and downwards, there still are some uncertainties. For instance, the effect of wobble may lead to uneven distribution of fuel among the holes, and therefore differences in spray formation and even plume-to-plume interactions. Other factors that may affect the shape of the rate of injection and so the mixture formation are the time evolution of the upstream pressure (related to the injector dynamics) together with the detailed geometry of the needle and its seat. Experimentally addressing these issues nowadays remains challenging, if not impossible, so Computational Fluid Dynamics (CFD) are used to study this phase of the injection process. Large Eddy Simulations (LES) are selected to account for the effects of turbulence. Volume-of-Fluid (VOF) approach is used, not only to analyze the flow inside the nozzle, but also the first 2-5 mm of the spray. Homogeneous Relaxation Model (HRM) is employed to consider the mass exchange between liquid and vapor phases of the fuel inside the nozzle, if necessary. The Spray G operating condition of Engine Combustion Network (ECN) is used in this analysis. Statistics of several realizations are performed in order to extract significant conclusions. Results are validated against experimental data, and show the effects of the turbulence in the spray development. A strong interaction between jets, especially in the transitory phases of the simulation (opening and closing), is observed. Spray parameters, after averaging the different realizations, also accurately match the experimental results and

Payri et al. "Transient nozzle flow analysis and near field characterization of gasoline direct fuel injector using Large Eddy Simulation," Int. J. Multiph. Flow, vol. 148, no. December 2021, p. 103920, 2021. DOI: 10.1016/j.ijmultiphaseflow.2021.103920

previous simulations reported in the literature. One of these precisely captured effects is the deviation of the spray from the geometric axis of the orifice.

Keywords: GDi, CFD, Nozzle flow, Transient, LES

1. Introduction

The concern about climate change, air pollution and the availability of fuel resources, along with the high demand for automobiles and transport vehicles, have led governments to regulate the level of pollution and CO_2 emitted by engines to the atmosphere. To comply with these regulations, vehicle manufacturers have introduced hybrid and electrified automotive powertrain architectures. On the other hand, the new homologation agreements which include expanded test conditions in terms of altitude and temperature, as well as longer and more rigorous specifications, lead to an increase in the performance requirements for injectors (Shi et al. (2018)). The problem of the rising restrictions together with the new injector requirements have developed a new challenge for researchers working in the engine industry whose current objective is to find the optimum injector configuration which allows complying with the new regulations. The fuel injection system, as well as the injection strategy, are determinant to obtain the optimum mixture between phases. Due to this reason, modern spark-ignition (SI) engines optimize the fuel injection process to prepare a correct air-fuel mixture distribution which leads to efficient combustion. Regargind the fuel economy and CO_2 emissions, gasoline cannot outperform diesel, although it stands out in terms of reducing toxic emissions such as CO and HC. For this reason, Gasoline Direct injection (GDi) technology is currently numerically and experimentally investigated with significant interest. One of the main characteristics of Gasoline Direct injection is the capability to inject the fuel directly into the combustion chamber which allows it to operate at higher compression ratios with richer fuel-air mixtures. The implementation of this technology enables an efficient combustion process that results in a reduction in the pollutants and better fuel economy (Zhao (2010)). Furthermore, this injection system allows the reduction of pump losses, knock effects and an improvement in the engine thermal efficiency. In spite of all this, GDi engines continue to have certain disadvantages such as tip wetting (Medina et al. (2020)) which leads to soot formation and the generation of particulate matter (PM) emissions

(Raza et al. (2018)).

Nowadays, GDi technologies are characterized by the reduced size of the orifices (in the order of a few hundred microns) and the high values of pressure and velocity (between 10-40 MPa and 150-300 m/s). The spray distribution and atomization are mainly influenced by the in-nozzle flow (Agarwal and Trujillo (2020)). Furthermore, the complexity of the GDi nozzle geometries designed commonly as multi-hole valve covered orifice (VCO) joined to the operation conditions leads to hole-to-hole variation (Grover et al. (2016), Duke et al. (2017)). There are many researchers who have dedicated their efforts to study in detail the geometry of this type of injectors. Matusik et al. (2017) obtained by means of the X-ray technique the geometry of an eight-hole counterbore type injector. Key geometry parameters such as the diameter of the holes, hole inlet corner radius and the diameter of the counterbore were identified by means of linear regression techniques. Duke et al. (2015) analyzed the asymmetric spray structure obtained by tomography when the orifice definition is changed from solid-cone to hollow-cone. The spray plumes are dependent on features of nozzle geometry such as needle lift, holes dimensions and L/D ratio. Noteworthy are the experimental analyses carried out in which the injector has been characterized under a wide range of operating conditions (Payri et al. (2016), Payri et al. (2015)). Moreover, studies based on the analysis of the spray shape, penetration and the behaviour of the jet when it comes out of the nozzle should also be highlighted (Li et al. (2019), Lee and Park (2014)).

On this context, Computational Fluid Dynamics (CFD) is a unique tool to expose the phenomena of interest at in- and near- nozzle regions. With the aim of creating a benchmark for both experimental and computational validations, a multi-hole direct fuel injector was made available by the Engine Combustion Network (ECN). Throughout these last years, computational studies have been done in parallel with experimental research in order to model in detail the flow of the internal nozzle (Saha et al. (2016b), Guo et al. (2020)) under different conditions, flashing and non-flashing. As near nozzle region is concerned, most of the research has been devoted to quasi-steady main injection phase using a long pulse duration to avoid the dependency on the transient conditions and to get convergence statistics. The jet throughout the injection process is influenced by flow oscillations, large turbulent and vortex structures, shear stresses and cavitation resulting in fast spray atomization (Torregrosa et al. (2020)). Because this phase plays an important role in understanding how the flow evolves during needle closure, it

remains as an important subject of investigation. However, little information is available on the opening transient phase where the flow begins to develop or the closing phase which is affected by the phenomena that take place during the injection. Nevertheless, and due to its relevance in the spray formation specially for short injection duration, it is being studied by several institutions (Yue et al. (2020)). CFD analysis goes beyond developing LES simulations (Zamani et al. (2016)) to model the injection process in order to avoid uncertainties that could be added to the results due to the use of Reynolds-Averaged Navier-Stokes (RANS) approach. In the current work, a computational study of the internal nozzle flow and near-nozzle during the whole injection will be performed. The consideration of turbulence will be improved using LES model in order to analyze the characteristics of the GDi spray formation during the injection process. The first part of the study will evaluate the mesh quality to ensure precision in the results. The injector will be characterized in terms of mass flow rate and momentum flux. The results will be compared to the experimental data available in the literature and the values obtained in previous works of this group from RANS simulations. The second part of this study will evaluate the deviation in the plume direction in comparison with the geometric angle (drill angle) and the spray angle using a new processing methodology.

2. Methodology

The methodology for the present research is based on the solution of the Navier-Stokes equations for a homogeneous multi-phase mixture. The unclosed non-linear term is modeled using the LES method. Mass transfer due to cavitation or flash boiling is treated by means of the HRM. The liquid-gas system has been addressed using an interface-capturing VOF description. More details about the employed models can be found in the validation work carried out by Zhao et al. (2014), Xue et al. (2014) and Battistoni et al. (2014).

2.1. Governing equations

The multi-phase fluid inside the nozzle and the near-nozzle spray is simulated in an Eulerian framework using a single-fluid approach governed by the classical conservation equations for mass, momentum and energy (Ferziger and Peric (2002)), Equations 1, 2 and 3 correspondingly defined as,

$$\frac{\partial \rho}{\partial t} + \nabla \cdot (\rho \vec{v}) = 0 \tag{1}$$

$$\frac{\partial \rho \vec{v}}{\partial t} + \nabla \cdot \rho \vec{v}\vec{v} = -\nabla p + \nabla \cdot \bar{\bar{\tau}} + \rho \vec{f} + \vec{F}_{sf} \tag{2}$$

$$\frac{\partial \rho e}{\partial t} + \nabla \cdot \rho e \vec{v} = -p \nabla \cdot \vec{v} + \bar{\bar{\tau}} \cdot \nabla \vec{v} + \nabla \cdot (K \nabla T) + \nabla \cdot (\rho D \Sigma_i h_i \nabla Y_i) \tag{3}$$

where ρ is the density, $\vec{v}$ is the velocity, p is the pressure, e is the internal energy, $\bar{\bar{\tau}}$ is the mixture stress-strain tensor due to molecular and turbulent viscosity, K is the molecular and turbulent conductivity, D is the molecular and turbulent diffusion coefficient, h_i is the species enthalpy and Y_i is the mass fraction of each species.

There are several methods to solve the overall set of equations. The one selected for this approach is the finite volume method. Transport equations are solved sequentially using a pressure-velocity coupling iteration method known as Pressure Implicit with Splitting of Operators (PISO). Transported quantities are located at the center of the cell which can result in a decoupling pressure-velocity. Rhie-Chow algorithm (Rhie and Chow (1983)) is used to prevent the mentioned effect. The discretization scheme used for computing the convection flux in density, energy, species and passives transport equations is first-order upwind scheme whereas the second-order central difference discretization scheme is used for the momentum. Better numerical stability is obtained using a successive over-relaxation (SOR) algorithm. The time-step is controlled by the Courant-Friedrichs-Lewy (CFL) ans results between $5 \cdot 10^{-7}$ and 10^{-10} s. Values for velocity-based Courant-Friedrichs-Lewy (CFL) are below 0.5 and below 10 for speed-of-sound-based CFL.

In the multi-phase system, three different species are considered for the current analysis: a liquid phase (subindex 1), a vapor phase (subindex 2) and the ambient non-condensable gas (N_2) (subindex 3). The mixture density is computed as the weighted average of each component densities and it is expressed through the following equation:

$$\rho = \alpha_1 \rho_1 + \alpha_2 \rho_2 + \alpha_3 \rho_3 = \alpha_g \rho_g + (1 - \alpha_g) \rho_l \tag{4}$$

being α_i the volume fraction of each component and the subindex g the sum of vapor and non-condensable gas (N_2).

For this application, the void fraction is not solved with an explicit transport equation. Individual species are solved first through the species mass

fraction transport equation, and then the void fraction is calculated (it is not transported directly). The species transport equation could be expressed as:

$$\frac{\partial \rho Y_i}{\partial t} + \nabla \rho Y_i \vec{v} = \nabla(\rho D_i \Sigma_i \nabla Y_i) + S_i \tag{5}$$

in which D_i is the diffusivity coefficient associated to each mixture component and S_i corresponds to the source term related with the mass transfer as a result of phase change. Finally, the void fraction α_g takes the form,

$$\alpha_g = \frac{Y_g/\rho_g}{\Sigma Y_i/\rho_i} \tag{6}$$

The gas-phase densities are obtained according to the equation of state for an ideal gas, being R_i the gas constant and T the temperature,

$$\rho_i = \frac{p}{R_i T} \tag{7}$$

For the present study, the inteface-capturing method known as Volume-of-Fluid (VOF) is selected to simulate the two-phase (liquid and gas) flow inside and near the nozzle. In order to compute the void fraction of each cell, the VOF method defines a function α_g. Those cells which are filled with only liquid will correspond to $\alpha_g = 0$ whereas the value of $\alpha_g = 1$ represents cells filled with only gas. Therefore, α_g between 0 and 1 refers to cells filled with a mix of liquid and gas species. Battistoni et al. (2015) present a detailed description of the employed approach.

The turbulent flow is modeled using the LES method in which the fields are decomposed into a resolved field and a sub-grid field. First of all, the spatial filtering operation is applied. Then, the unclosed non-linear term of the Navier-Stokes equation must be modeled. The filtered transport equation of momentum (Equation 2) is shown as the following:

$$\frac{\partial \bar{\rho}\widetilde{u_i}}{\partial t} + \frac{\partial \bar{\rho}\widetilde{u_i}\widetilde{u_j}}{\partial x_j} = -\frac{\partial \bar{P}}{\partial x_i} + \frac{\partial \bar{\sigma}_{ij}}{\partial x_j} - \frac{\partial \tau_{ij}}{\partial x_i} \tag{8}$$

Terms with '$-$' and '$\backsim$' are the filtered quantities obtained through the Reynolds filtering and Favre-filtering, respectively. Density (ρ) and pressure (p) are Reynolds filtered, whereas velocity (u_i) and other thermodynamics variables are Favre-filtered to consider the compressibility of the fluid (Pope (2009)). τ_{ij} is the stress flux tensor at the sub-grid scale and needs to be closed by an additional sub-grid model. σ_{ij} is the stress tensor expressed by,

$$\bar{\sigma}_{ij} \cong \widetilde{\sigma}_{ij} = \mu(\frac{\partial \widetilde{u}_i}{\partial x_j} + \frac{\partial \widetilde{u}_j}{\partial x_i}) - \frac{2}{3}\mu\frac{\partial \widetilde{u}_k}{\partial x_i}\delta_{ij} \tag{9}$$

The sub-grid stress tensor (τ_{ij}) is an independent quantity defined according to the One-Equation Viscosity Model (Yoshizawa and Horiuti (1985), Menon et al. (1996)). This LES sub-grid model adds one additional transport equation for sub-grid kinetic energy and is characterized for using the sub-grid kinetic energy in modeling the turbulent viscosity. The sub-grid kinetic energy transport equation is given by:

$$\frac{\partial k}{\partial t} + \bar{u}_i\frac{\partial k}{\partial x_i} = -\tau_{ij}\frac{\partial \bar{u}_i}{\partial x_j} - \epsilon + \frac{\partial}{\partial x_i}(\frac{\nu_t}{\sigma_k}\frac{\partial k}{\partial x_i}) \tag{10}$$

Here the sub-grid kinetic energy is defined as;

$$k = \frac{1}{2}(\overline{u_i u_i} - \bar{u}_i\bar{u}_i) \tag{11}$$

The model for the sub-grid stress tensor is,

$$\tau_{ij} = -2\nu_t\bar{S}_{ij} + \frac{2}{3}k\delta_{ij} \tag{12}$$

where the turbulent viscosity, ν_t, is given as:

$$\nu_t = C_k k^{1/2}\Delta \tag{13}$$

being C_k a constant that can be adjusted by the user, defined as 0.05 for the present study (Menon et al. (1996)). In this framework, Δ is defined as the grid filter and its size and shape are fixed by the computational cell, therefore the filter type is a box for this analysis. The sub-grid dissipation is defined as

$$\varepsilon = \frac{C_\varepsilon k^{3/2}}{\Delta} \tag{14}$$

In the same way as the turbulent viscosity, the sub-grid dissipation can be tuned by adjusting the constant C_ε in the previous equation. For the current research, the value is set equal to 1 following the recommendations of Yoshizawa and Horiuti (Yoshizawa and Horiuti (1985)).

It is worth mentioning that the choice of this sub-grid model for modeling the unclosed non-linear term of the Navier-Stokes equation is the result of

previous studies carried out by this group (Payri et al. (2021)). In the mentioned research, two sub-grid models were compared, the Dynamic Structure model selected as one of the best sub-grid models in engine applications and the One-Equation Viscosity model noted for its accuracy in coarse mesh analysis. Although both approaches add a transport equation for the sub-grid kinetic energy, the calculation of the sub-grid stress tensor is different. While the One-Equation Viscosity model uses the turbulent viscosity to model the sub-grid stress tensor, the Dynamic Structure approach models the sub-grid stress tensor as a function of the sub-grid turbulent kinetic energy. From the research, it can be said that similar results were observed for rate of injection (ROI) and rate of momentum (ROM) variables in both approaches, although the Dynamic Structure tends to provide slightly higher results than the One-Equation Viscosity model, namely 2%. Looking at mixing and atomization, both models addressed similar values, so neither stands out from the other. Finally, analyzing the quality of the mesh, the Dynamic Structure model, although not far away, falls below the limits established to ensure the accuracy of the results. Therefore, for a specific meshing strategy and based on the results obtained, the One-Equation Viscosity sub-grid model is preferred and has consequently been the model chosen for this study

2.2. Liquid-Vapor Mass Transfer Model

Mass transfer due to phase change normally takes place between the liquid phase and its vapor. The model for heat and mass exchange between liquid and vapor phases of the same species is based on the non-equilibrium homogeneous relaxation model (HRM) (Bilicki and Kestin (1990)). Although HRM was firstly developed for one dimensional analysis, Schmidt et al. extended this model to a two-dimensional and three-dimensional models (Schmidt et al. (1999), Schmidt et al. (2010)). This mass transfer model is capable of computing vaporization processes driven by pressure drop, referring to both cavitation and flash-boiling. In cavitation process which is considered to be very fast, phase change usually takes place at low temperatures (low superheating is required) because of sudden pressure drop. Whereas flash-boiling occurs at higher temperatures with lower pressure drop in a relatively longer period of time compared to the cavitation phenomenon.

HRM model describes in a synthetic way the rate at which the instantaneous vapor mass fraction tends toward its equilibrium value. The rate equation which defines this concept takes the form,

$$\frac{Dx}{Dt} = \frac{\bar{x} - x}{\Theta} \tag{15}$$

being x the instantaneous mass fraction (Equation 16) and $\bar{x}$ the equilibrium quality, function of the thermodynamic properties at the local pressure and determined as Equation 17.

$$x = \frac{Y_{vap}}{Y_{vap} + Y_{liq}} = \frac{m_{vap}}{m_{vap} + m_{liq}} \tag{16}$$

$$\bar{x} = \frac{h - h_{l,sat}}{h_{v,sat} - h_{l,sat}} \tag{17}$$

where h is the fluid enthalpy of liquid and vapor mixture (without taking into account the non-condensible gas (N_2) content) and $h_{l,sat}$ and $h_{v,sat}$ are the saturated liquid and vapor enthalpy, respectively. The time-scale Θ is evaluated with the following equation,

$$\Theta = \Theta_0 \alpha^a \psi^b \tag{18}$$

where $\Theta = 3.84 \cdot 10^{-7}[s]$, α is the fuel void fraction, $a = -0.54$ and $b = 1.76$ [28]. Values of a and b are chosen following the study developed by Saha et al. (2016a) in which the model constant values were tested for a GDi application. ψ is a dimensionless pressure defined by

$$\psi = \left| \frac{p_{sat} - p}{p_{crit} - p_{sat}} \right| \tag{19}$$

where p is the global pressure, and subindices *sat* and *crit* refer to saturation and critical pressure of the fluid, respectively.

For the present case, it is necessary to include the phase change model as this phenomena can lead to changes in fluid velocities. The operating conditions of this study, as cited in the next section, are not favorable for the appearance of the well-known flash boiling or cavitation. The combined effects of the particular GDI nozzle geometry, the low needle lift and the low vapor pressures of the fuels typically used are what may, however, enhance the importance of these phenomenon.

2.3. Geometry and Test Condition Description

The aim of the present study is to contribute to the Engine Combustion Network (ECN) in the generation of a huge benchmark in the direct injection systems (Mohapatra et al. (2020), Pickett et al. (2020)). Therefore, the analysis is based on a GDi injector known as Spray G and operating conditions stipulated by the mentioned group. One aspect to highlight of the ECN is that it not only characterizes gasoline injectors but also diesel ones, thus generating a database of measurements and input parameters necessary for modelers to carry out their research (Pandal et al. (2020), Cordier et al. (2020), Navarro-Martinez et al. (2020), Mohan et al. (2020)). The Spray G injector selected for the study is solenoid driven with a valve covered orifice (VCO) nozzle. It is a 8-hole injector with counter-bore shape in its orifices. In addition, a remarkable feature of this injector is that it has 5 needle guides on the nozzle wall which reduce the mass flow passage. Despite this, the injector can be considered symmetrical in the plane that includes holes numbered as 1 and 5 (Baldwin et al. (2016)) (Figure 1). Figure 1 shows the distribution of the holes which is important to know since the existence of these dimples can affect the distribution of flow in the holes causing variations from one to another. It is known that the use of LES models, as is the case of the current research, increases the computational cost of the simulation since the cell sizes used for the analysis are much smaller than in the RANS case. In order to save computational cost, only half of the geometry will be simulated. The analyzed geometry has been obtained from x-rays together with their corresponding post-processing (Duke et al. (2017)). The characteristics to emphasize of the injector are its nominal diameters 165 µm and 388 µm respectively and its ratio between the length and diameter of the nozzle holes counter-bored between 1 and 1.2.

Surrogate fuels have been chosen over the years to study the behavior of gasoline in a simplified way. These fuels contain a limited number of pure components blended together to achieve combustion and emission characteristics. For the current work, a mono-component fuel, iso-octane (2,2,4 trimethylpentane), has been used. Regarding the operating conditions, the study is based on the standard ECN condition called with the same name as the injector, Spray G and summarized in detail in Table 1. This condition is defined as a non-flashing owing to the back pressure used in the downstream region is higher than the saturation vapor pressure of the fuel (Moulai et al. (2015)). Nonetheless, due to the fact that temperature of the chamber is higher than the fuel temperature and convective heating occurs, evaporation

of the liquid is expected. Concerning the cavitation phenomenon, one of the parameters favoring this physical process is high pressure differences which are not so common for GDI operation unlike diesel conditions (Desantes et al. (2003), Payri et al. (2004)). However, it should also be noted that another factor promoting cavitation are inlet corner radius of straight orifices, such as those in the nominal Spray G geometry. The standard Spray G condition is not known to generate cavitation throughout its steady state operation. Nevertheless, it is necessary to pay attention to the transient opening and closing phases where cavitation and gas ingestion phenomena become more pronounced and can affect spray geometry, atomization and mixing as well as spray direction.

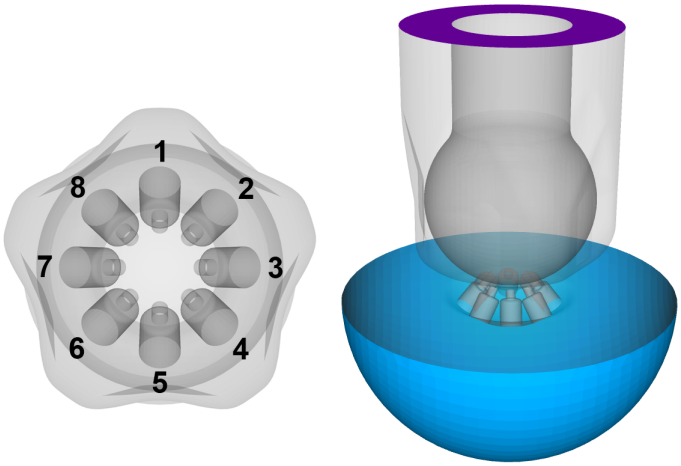

Figure 1: Sketch of the nozzle geometry with the numbered holes besides the computational domain used for the CFD simulation.

2.4. Computational Domain and Mesh

Figure 1 shows the computational domain of the simulations. The outlet (colored in blue in the image) is a semi-spherical surface with a diameter of 6 mm. This distance is considered enough to avoid the effects of the outlet boundary condition as shown previous research of this group (Payri et al. (2019)).

All simulations have been performed in the software CONVERGE v2.4. The inlet boundary (purple color in the figure) has been modeled applying a fixed value pressure boundary condition and zero gradient for velocity.

Parameter	Spray G
Injection pressure (p_i)	20 MPa
Injection temperature (T_f)	363 K
Ambient pressure (p_a)	0.6 MPa
Ambient temperature (T_a)	573 K
Ambient density (ρ_a)	3.5 kg/m^3
Ambient gas	Nitrogen

Table 1: Test matrix of injection conditions for both experiments and simulations.

Temperature has been defined as a stipulated value corresponding to the fuel operating condition. Walls, identified as transparent grey in Figure 1, have been designated as non-slip conditions and their corresponding boundary layers modeled using the Werner and Wengle wall function. A zero normal gradient condition for velocity is defined for the outlet boundary. In this boundary, pressure and temperature have a fixed value according to the operation conditions. Regarding the turbulence boundary conditions, the use of LES models, One Equation in this particular case, allows to initialize only the turbulent kinetic energy defined through the turbulent intensity with a value of 0.01.

For the purpose of initializing the simulation, the nozzle as well as orifices are filled with liquid fuel (iso-octane) at the injection temperature (363K). The nozzle is defined at a constant pressure equal to the injection pressure (200 bar) but the orifices are at a pressure comparable to that of the discharge chamber (6 bar). On the other hand, the outlet plenum is filled with non-condensable gas (nitrogen) at constant discharge pressure (6 bar) and temperature (573 K). The compressible liquid density correlation has been defined as Equation 20 using a reference pressure (101325 Pa), reference density (688.5 kg/m^3) and bulk modulus (5.3E08) obtained from the study of Dymond et al. (1985). The viscosity of the liquid is defined from Sutherland's Law. Other liquid and gaseous species have been specified as compressible and the material properties used were obtained from the software's own database for iso-octane (Richards et al. (2018)). Both gaseous phases are treated on the basis of the equation-of-state of ideal and perfect gases.

$$\rho_{liq} = 688.5e^{\left(\frac{P_{inj}-101325}{5.3E08}\right)} \tag{20}$$

The scope of the current work involves transient simulations. In order to simulate this motion, the surface of the needle follows the averaged needle lift profile provided by Argonne National Laboratory (Duke et al. (2017)) (Figure 2). The wobble movement has not been considered for this approach because only half of the geometry is analyzed. Furthermore, previous research like the work of Duke et al. (2017) or those carried out in this institute (Shahangian et al. (2020)) demonstrated that it could be neglected due to its little influence. Since there is no sealing algorithm, a minimum space is required between the needle and its seat. A value of 2 µm is used for the "closed" position of the needle and the start and end of the injection.

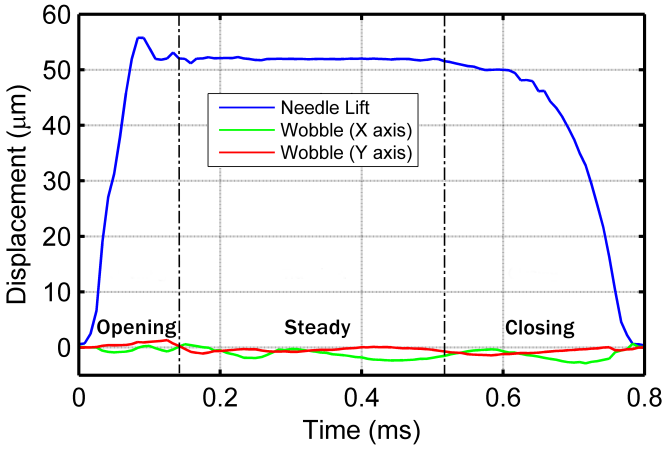

Figure 2: Averaged needle lift and wobble profile provided by Argonne National Laboratory (Duke et al. (2017)) divided into the different study sections.

Regarding the mesh, the use of LES models implies a high dependency on cell size in energy modeling. Several studies such as the ones performed by Keskinen et al. (2016) indicate that the use of a moving mesh in LES can influence the statistics in a manner that is not directly related to the mesh resolution. One of the variables that is most affected and hence most sensitive to changes in the mesh is the RMS (Root Mean Square) of the fluctuating velocity, especially in the tangential and radial components. Therefore, it has been adopted a fixed mesh for the study. The choice of the mesh sizes and refinements are based on compliance with the quality criteria explained

in the following Section 2.6. Figure 3 shows the final configuration. The selected base size is 135 µm which has been refined through fixed embedding of 8.44 µm. The minimum cell size takes place in the needle seat where the main pressure drop occurs and has a value of 4.22 µm. The resulting mesh has a total of 22.4 million of cells which represents only half of the domain due to the symmetric condition.

It is necessary to mention with regard to the mesh that, during the initial time steps, the minimum distance between the needle and the nozzle only allows the presence of one cell among them, which can give rise to certain limitations in the initial simulation times. However, the opening ramp has a very steep slope, so this problem would occur in only 5% of the total time it takes for the opening phase. In addition, the velocity gradients at these times are not large enough to generate major discrepancies in the results. Therefore, the aforementioned shortcomings, if any, would be minimal and controlled, not significantly affecting the results and findings of the simulations.

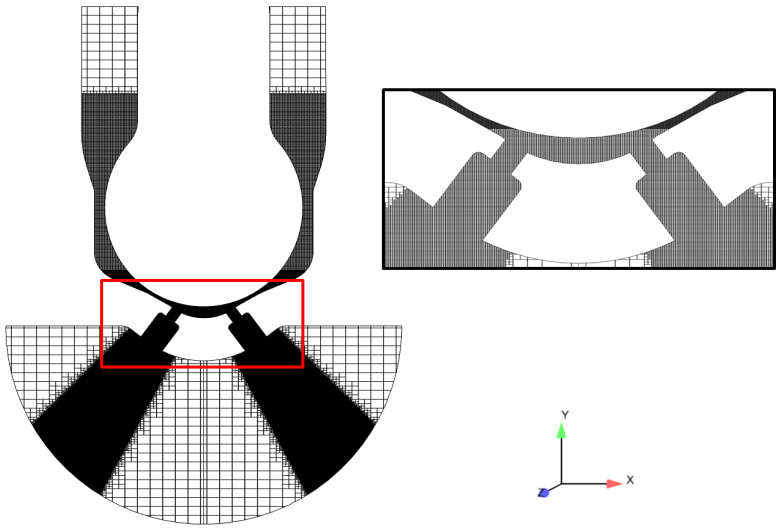

Figure 3: Vertical cross section of the tetrahedral mesh with 6 mm outlet domain and cone-shaped refinement strategy.

2.5. Hydraulic characterization of the nozzle

The most widespread and consistent way to analyze the internal nozzle flow is from mean parameters measured at the orifice outlet and dimensionless

flow coefficients such as discharge, velocity or area coefficients, among others. The dimensionless coefficients defined by Payri et al. (2016) that describe the behavior or characteristics of the flow inside the injector are as follows:

- **Discharge coefficient**. This coefficient is defined as the real mass flux with regard to the maximum theoretical mass flux. The maximum mass flux is evaluated considering uniform velocity obtained from Bernoulli's theorem and the cross-section of the outlet orifice.

$$C_d = \frac{\dot{m}}{\dot{m}_{th}} = \frac{\dot{m}}{A_o \rho_f u_{theoretical}} \tag{21}$$

- **Momentum coefficient**. In the same way, the momentum coefficient relates the theoretical momentum obtained from the Bernoulli velocity to the actual measured momentum.

$$C_M = \frac{\dot{M}}{\dot{M}_{th}} = \frac{\dot{M}}{A_o \rho_f u^2_{theoretical}} = \frac{\bar{\dot{M}}}{2A_o \Delta p} \tag{22}$$

- **Velocity coefficient**. This coefficient relates the effective velocity to the maximum theoretical Bernoulli velocity. It is calculated with the following equation,

$$C_v = \frac{u_{ef}}{u_{theoretical}} = \frac{u_{ef}}{\sqrt{2\Delta p/\rho_f}} \tag{23}$$

- **Area coefficient**. The coefficient is used for evaluating the reduction of the effective area with regard to geometric one, and it is calculated as

$$C_a = \frac{A_{ef}}{A_o} \tag{24}$$

2.5.1. Relations between coefficients

Once the dimensionless coefficients defining the flow inside the nozzle have been established, it is of interest to know the relationships between them. Substituting into Equation 21 the value of the mass flux in function of the effective parameters, Equation 25 is

$$C_d = \frac{A_{ef}\rho_f u_{ef}}{A_o \rho_f u_{theoretical}} \tag{25}$$

Now, combining the Equation 25 with Equation 23 and Equation 24,

$$C_d = C_a C_v \tag{26}$$

Operating in the same way with the momentum coefficient it is obtained

$$C_M = C_a C_v^2 \tag{27}$$

Finally, merging the latter two relations it is obtained

$$C_v = \frac{C_M}{C_d} \tag{28}$$

2.6. LES quality assessment

The grid resolution and the modeling of the small scales affect the turbulent resolution in scale-resolved large eddy simulations (LES). This type of models are characterized by modeling part of the turbulence flow energy which means that the local grid size and the numerical method employed have a clear influence on the degree of contribution of the model. The grid resolution is an important factor to consider because it not only affects the numerical discretization error but also the subgrid scale model contribution as mentioned above. The interest of CFD researchers in the implementation of LES models in order to analyse the phenomena that take place in the injection process has been increasing over the years. The application of these models requires a quality assessment to ensure enough resolution of the turbulent flow energy and precise LES results (Zamani et al. (2016)). In order to quantify the reliability of the LES model implemented, several authors defined indexes of quality in terms of both numerical and model accuracy (Meyers et al. (2003), Geurts and Fröhlich (2002)). For the current work, the criterion selected to determine the quality of the model will be one of the most widespread on the basis of viscosity defined by Celik et al. (2005).

- *Index based on the viscosity (IQ_v)*: this criterion evaluates the contribution relative to the laminar viscosity (υ), the sub-grid viscosity (υ_{sgs}) and the numerical viscosity (υ_{num}) according to Equation 29. Celik et al. (2005) suggested that IQ_v values between 0.75 and 0.85

are acceptable, which means at least 75% of the turbulent kinetic energy is resolved, because that can ensure appropriate LES quality for High-Reynolds-number flows.

$$IQ_v = \frac{1}{1 + \alpha_v(\frac{s^*}{(1-s^*)})^n} \tag{29}$$

where s^*, always lower than 1, can be defined by Equation 30.

$$s^* = \frac{\langle v_t \rangle + \langle v_{num} \rangle}{\langle v_t \rangle + \langle v_{num} \rangle + \langle v \rangle} \tag{30}$$

The two constants which appear in Equation 29 have been calibrated at $\alpha_v = 0.05$ and $n = 0.53$ based on DNS outcomes (Celik et al. (2009)). The evaluation of $s*$ requires the calculation of turbulent statistics. The present case has been divided into three different parts when simulating, as shown in the Figure 2. The quality index for the steady part of the simulation (from 0.15 to 0.51 ms) has been analyzed from time-averaged variables. By contrast, the opening and closing phases cannot be averaged over time. For this reason, the quality index has been extracted at each time-step for the transient phases of the simulation, opening and closing. In the current study, several simulations have been carried out with the aim of comparing the results with those obtained by Reynolds-Averaged Navier-Stokes (RANS) approaches. Therefore, the accuracy of the previous assumption could also be verified. Results obtained from the computed IQ_v criterion affirm that the index requirement is globally satisfied inside the injector and the discharge chamber. Figure 4 graphically shows the results achieved and prove the conclusion extracted, providing acceptable critical index values that evidence the reliability and quality of the simulation.

3. Results

This section includes the validation of the results obtained from the internal nozzle flow study and compares them with existing data from previous studies carried out by CMT-Motores Térmicos and published in the ECN network. The parameters referred to for validation and which are available in the literature are the mass flow rate and the momentum flux.

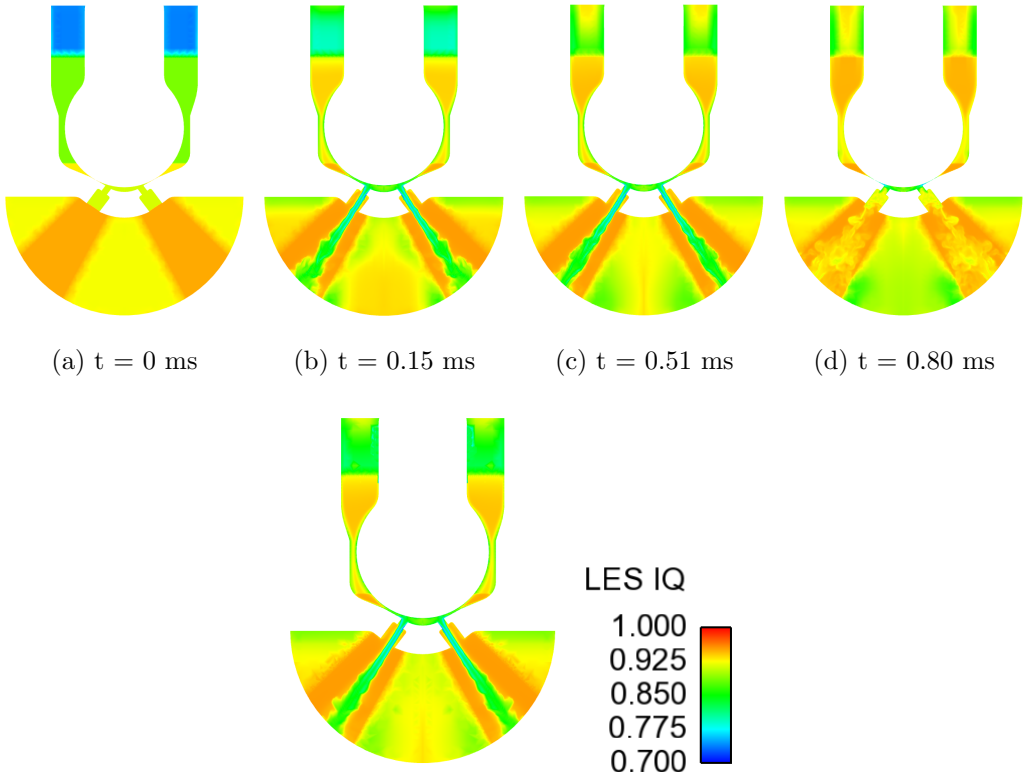

(a) t = 0 ms (b) t = 0.15 ms (c) t = 0.51 ms (d) t = 0.80 ms

(e) Time-averaged (from 0.15 to 0.51 ms)

Figure 4: LES quality assessment using an index based on the viscosity evaluated in several time-steps and time-averaged results.

As it is mentioned in previous sections, this analysis has been conducted in three different phases (see Figure 2). Firstly the opening slope, secondly the stationary part of the simulation where the needle is kept at its highest point and finally the closing process has been simulated. Both the opening and closing of the needle are considered to be rapid and time dependent. Since the approach used to cope with turbulence is LES, a sample size study has been carried out to determine how many simulations would be needed to compare the results with those obtained from RANS approaches. The sample size is base in the following equation: $n = \left(\frac{Z\sigma}{e}\right)^2$ where Z is the statistical

confidence level, σ the standard deviation and e the assumed error. For this analysis a statistical confidence level of 95% has been considered while the error used for the calculation is limited to within 5% of the average variable analyzed. The present study has been carried out for two macroscopic variables such as rate of injection (ROI) and rate of momentum (ROM). The obtained conclusions are the same for both variables, so only the mass flow rate has been represented in the Figure 5.

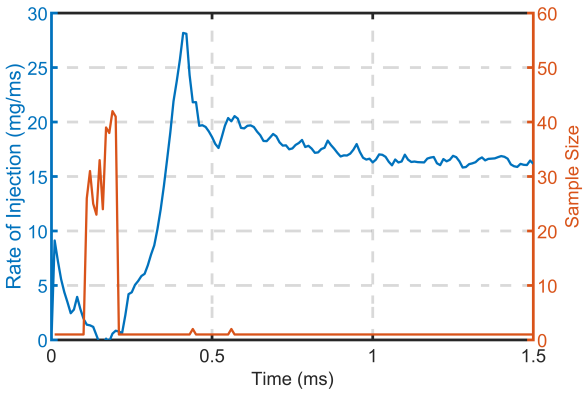

Figure 5: Sample size related to the injection rate for the times involved during the needle opening process.

Figure 5 shows the results obtained from the sample size and relates them to the rate of injection for the times involved during the needle opening process. Until 0.2 ms after Star-of-Injection (aSOI), it can be seen that there is an area where the sample size shows its maximum. This is due to the low values of mass flow rate and the similarity between simulations, which results in small standard deviation and, above all, low assumed error. After that, when ROI is not close to zero, the sample size is reduced having a maximum value of 3. This means that the sample size required to obtain accurate results does not exceed 3 simulations for this kind of research. It is also worth mentioning that the existing standard deviation in the ROI and ROM variables between simulations has been calculated. The difference is so small that it can be assumed that a single simulation is sufficient if the study is focused on macroscopic variables.

In order for this statement to take strength, the fluctuations of the fluid were analyzed using the room mean square velocity variable ($\tilde{u}'_{rms}$). The study has been carried out in the opening phase and the results obtained for a

time close to half of the needle opening, t = 0.075 ms, are presented in Figure 6. The computation of the studied parameter has been performed using 2, 3 and 4 simulations. Figure 6 depicts the values of the variable $\tilde{u}'_{rms}$ for the three mentioned cases in a vertical plane over orifice 3 and in a horizontal plane at 1 mm from the tip of the injector. It can be immediately noticed that the difference between the results obtained with 2 and 3 simulations is significant, both in the shape of the variable and in the values of the same. However, if the results obtained with 3 and 4 simulations are compared, the difference is minimal and it could be said that it is not perceptible to the eye.

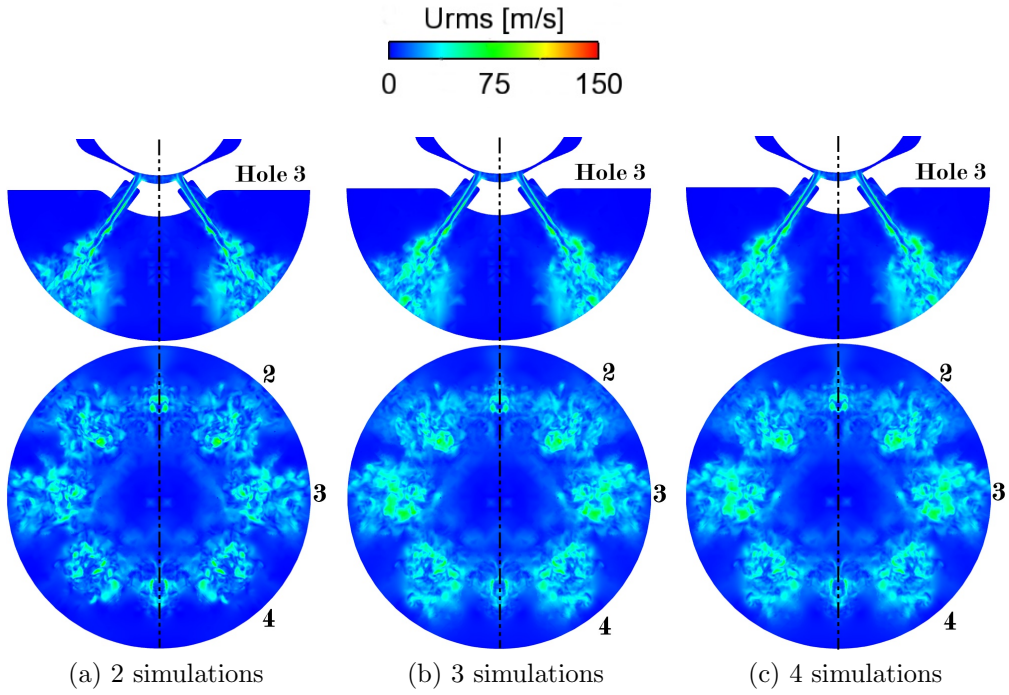

(a) 2 simulations (b) 3 simulations (c) 4 simulations

Figure 6: $\tilde{u}'_{rms}$ representation in a vertical cut plane through orifice 3 and in a plane at 1 mm from the tip of the injector at t = 0.075 ms.

In addition, to make the study more precise, a comparison of the $\tilde{u}'_{rms}$ obtained in the plane at 1 mm from the tip of the injector has been carried out for the three cases considered. To this end, the variable has been extracted in lines starting at the center of the plane and crossing the jets in the middle, or, in other words, in the lines resulting from intersecting the vertical

planes that cut each of the orifices with the horizontal plane at 1 mm. This research has been conducted for all orifices and the conclusions drawn can be considered similar for all of them. Figure 7 summarizes the data obtained from this analysis. As previously observed, the fluctuations captured with 2 simulations differ greatly from those obtained with 3 simulations. However, comparing the root mean square velocity obtained from 3 simulations with that of 4 simulations, it is noticed that the trends are the same, perfectly capturing the fluctuations of the variable for the three different sprays. It is true that in some specific points, the value of the variable differs from one case to another, but in no case is it greater than 8%. This statement again corroborates the results obtained from the sample size study, 3 simulations are enough to obtain accurate and comparable results with data available in the literature if a study is to be carried out beyond macroscopic variables.

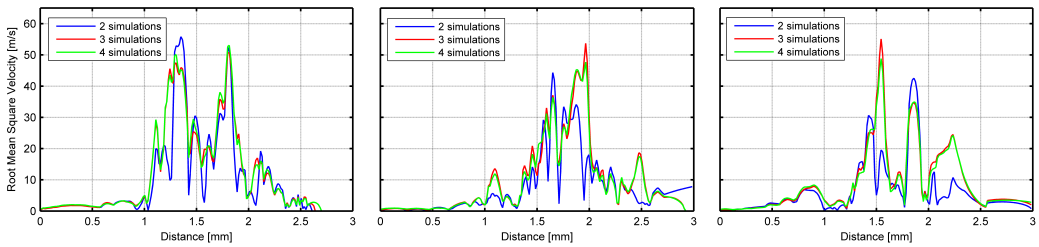

(a) Hole 2 (b) Hole 3 (c) Hole 4

Figure 7: $\tilde{u}'_{rms}$ comparison between different sample sizes using 2, 3 and 4 simulations at t = 0.075 ms for the three studied sprays.

Once the sample size required for the comparison has been analyzed, the results are validated with those obtained by means of RANS approximations and from experimental measurements (Payri et al. (2016), Payri et al. (2015)) in order to prove the accuracy of the computational simulations when the needle is in motion. Figure 8 displays the results obtained from this comparison for both rate of injection and rate of momentum. The computational profiles for the mass flow rate were generated by the flow through the perpendicular planes to the counter-bored orifices outlet. Whereas, the momentum flux has been measured in the same way as it has been experimentally done, at a certain distance from the tip of the injector (1 mm) capturing all the sprays together. It is important to mention that the shaded area in the experimental data corresponds to the equivalent of the standard deviation (STD) obtained from carrying out 50 repetitions of the same measurement.

In the early time of injection, Figure 8a illustrates that the computational results represent a faster opening for both approaches while the closing seems to be similar even in the LES results where a higher mass flow is available. It is observed that in both approaches, RANS and LES, the quasi-steady state is reached at 0.1 ms aSOI of injection. This quasi-steady condition is achieved before the needle lift reaches its maximum. This phenomenon has also been observed by other researchers and reflected in articles such as the one published by Yue et al. (2020).

As commented in Section 2, the injection pressure was set as a constant value and the minimum needle lift was settled at 2 µm. This justifies the effect that can be seen at the beginning of the simulation on the mass flow rate. At the opening phase, an expansion wave travels upstream of the injector nozzle which temporarily reduces the injection pressure. The duration and intensity of this wave depends not only on the fluid but also on the geometry of the injector. As in other studies (Yue et al. (2020)), the effect is appreciable in this particular injector for refined meshes and not for thicker ones. This outcome can be mitigated by the use of pressure ramps that evolve from ambient pressure to injection pressure as demonstrated in previous research of this group (Shahangian et al. (2020)). On the other hand, the experimental overshoot, which arises when the needle lift reaches it maximum, is well reproduced by both computational results being more pronounced in the case of the LES model.

During the period of time in which the needle lift remains in the steady lift, no significant variations are observed in the ROI results obtained with LES approaches due to the presence of vortices inside the counter-bore. Regarding the comparison between the ROI profiles, it can be observed that the estimation offered by the RANS model adjusts quite well to the experimental curve while the LES values overpredicts the results. In order to explain the existing overpredition, the time-averaged mass flow has been calculated in each of the holes following the present numbering in the Figure 1. Table 2 shows the results for the five compared holes. Small differences are observed in holes 2, 3 and 4 between both approaches but the main differences are found in holes 1 and 5. These holes coincide with the ones where the symmetry condition has been applied so that only half a hole is taken into account for the LES. This could mean that the symmetry condition is not adequately capturing the behavior of the fluid thus generating a higher flow and so an overestimation in the total mass flow rate. It is worth noting that, despite observing this behavior, the effect of the symmetry boundary condition on

holes 2, 3 and 4 analyzed in the paper is expected to be small (Fukagata et al. (1998), Yue et al. (2020)). Table 2 also reflects the experimental measured mass flow rate at standard Spray G conditions per orifice at steady state, which can be used to validate the present results. This value has been obtained by splitting the total mass flow rate result presented in Table 3 between the 8 existing orifices, which eliminates the possible and existing variation between orifices due to the asymmetry of the geometry upstream of the injector (Baldwin et al. (2016)). For the reasons mentioned above, only orifices 2, 3 and 4 will be taken into consideration. In the case of RANS simulations, the individual mass flow rate differences range between 2-4% while in the LES approach these discrepancies are between 4-6%. Both results obtained with RANS and LES approaches are considered reasonably good prediction taking into account the possible added experimental uncertainty when dividing the total result.

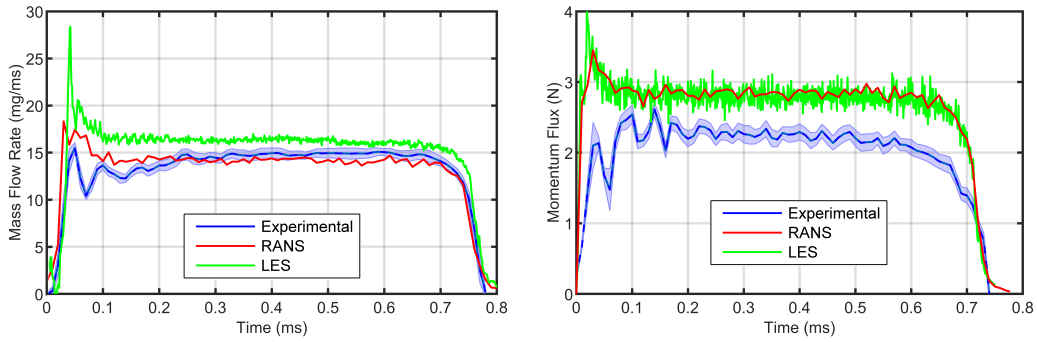

(a) ROI (b) ROM

Figure 8: Mass flow rate and momentum flux predictions for transient simulation compared with RANS solution and experimental measurements for Spray G condition.

After discussing the outcomes of the mass flow rate, Figure 8b shows the results for the momentum flux. As mentioned earlier, the computational results have been measured in the same way as the experimental results with the aim of being consistent in measurement. This means that the momentum rate has been measured on a plane perpendicular to the injector so that all sprays are captured. The mentioned configuration was used due to the low angle of the spray plumes compared to those of a diesel injector (Payri et al. (2016), Payri et al. (2015)). This causes the spray plumes to interact with each other an therefore it is difficult to separate the measurement of one

	RANS		LES	
	Time-Averaged [g/s]	STD [-]	Time-Averaged [g/s]	STD [-]
Hole 1	1.76	0.074	2.27	0.056
Hole 2	1.80	0.097	1.96	0.048
Hole 3	1.79	0.052	1.92	0.065
Hole 4	1.76	0.098	1.95	0.041
Hole 5	1.80	0.062	2.14	0.057
Experimental	1.84 ± 0.078 [g/s]			

Table 2: Holes mass flow rate comparison between RANS and LES approaches. Time-averaged measurements and standard deviation.

spray plume from the other. The frontal configuration allowed to measure all the spray plumes at the same time and have a global measurement.

Comparing the results obtained experimentally with both RANS and LES approaches, an overestimation of the momentum can be seen. For computational cases, the maximum distance is 1 mm since the discharge volume chosen for these analyses is 6 mm in diameter. For the experimental case, there is no limitation in the volume of discharge so that the momentum can be measured at various distances from the tip, taking as a reference the results at 2 mm for the comparison of this analysis. Theoretically, the momentum rate should be preserved, but some differences have been observed when this value is requested at different distances from the injector (Payri et al. (2015)). The variation in the data acquisition distance may be one of the reasons for the existing difference in the momentum flux values.

On the other hand, there are several uncertainties in the experimental momentum flux measurement. The first of these is related to the angle of impact of the sprays on the target, which must be known in order to make a correction of the measurements. Although some studies have been based on the characterization of the Spray G liquid spray and the calculation of the spray angle (Manin et al. (2015)), there are still some discrepancies in the literature. The other uncertainty is related to the air entrainment. The value in this configuration is unknown and unlikely to be perpendicular to the spray direction. This effect would cause the value measured to be different than what it should be. The air could take away momentum in the injector axis to provide it in the perpendicular axis where it cannot be measured.

The time average values of the rate of injection and the rate of momentum

	ROI [g/s]	ROM [N]	C_d	C_m	C_v	C_a
Experimental	14.71	2.63	0.55	0.40	0.73	0.75
RANS	14.25	2.84	0.53	0.43	0.81	0.65
LES	16.15	2.80	0.60	0.42	0.70	0.86

Table 3: Comparison between experimental and computational nozzle flow coefficients in the steady state period for non-flashing condition.

when the needle is completely open are used to compute the dimensionless nozzle flow coefficients described by Payri et al. (2016): the momentum coefficient (C_m), the discharge coefficient (C_d), the velocity coefficient (C_v) and the area coefficient (C_a). These coefficients characterize the flow capacity and hydraulic behavior of the nozzle. Table 3 summarizes the obtained results together with the mass flow and momentum rates in order to evaluate the activity of the injectors in a steady state and to further validate the simulations.

Low discharge coefficients are characteristic of this type of nozzles. This phenomenon is due to the fact that liquid fuel does not fill the holes, therefore most of the cross-sectional area of the holes is occupied by gas. The gas is not vapor fuel but rather an environmental gas (N_2 in this case) that is drawn inwards, creating strong recirculation areas inside the holes. The values of the velocity coefficient are also substantially low.

In the mass and momentum flow profiles, there were differences compared to the experimental results. These same effects are noticed in Table 3. The existing overestimation in the LES models is transferred to the dimensionless coefficients, giving a higher discharge, momentum and area coefficients, then underestimating the velocity coefficient. High effective area leads to a reduction in effective velocity. This means that the flow detachment occurring in the orifice is underpredicted by the LES approach while the RANS model overestimates this phenomenon.

Once the macroscopic variables of mass flow and momentum flux as well as the dimensional coefficients which define the hydraulic behaviour of the injector have been analyzed, the study of contours with different variables and vortex structures that make up the spray has been carried out. Figure 9 displays in detail the area near the injector exit as well as the structures and behaviour of the spray in the near-nozzle field. Figure 9a the variable α is represented by an isosurface where the dark part reflects the higher

concentration of liquid. In the same figure, the liquid mass fraction and the lines corresponding to the magnitude of the velocity are shown as contours. These visible contours correspond to two planes that are perpendicular to each other and pass through the middle of the spray. The core of the spray remains intact at the exit of the counterbore and as the flow develops it begins to mix with the ambient gas. The most remarkable effect of this image is the existing interaction between sprays that can be seen in the upper part of the image. The plume-to-plume interaction in gasoline direct injectors has been and is currently widely studied due to the ability this effect has to change the shape of the spray as well as its characteristics and the atomization process (Cheng et al. (2017)). In this specific simulation, the effect is noticeable when the needle is in its opening phase, in particular this image corresponds to 100 µm aSOI, and it is minimized when the needle opening evolves to a stationary state. Although the aim of this analysis is not to focus on the spray atomization process, it can be stated that adjacent sprays are necessary when the atomization phenomena that occur in this type of injectors are to be studied more in detail.

Figure 9b present a closer look at the near-nozzle region of the spray and vortex structures shown by the Q-criterion iso-surface and where the velocity has been plotted. The geometry used for this study is known as "nominal geometry" which has significantly different features from the real geometry. This geometry does not take into account the surface finish and defects so it has a prescribed smooth wall. Furthermore, these are not the only differences, the geometric characteristics of the hole, that is the diameter of the hole and the counter-bore as well as the length of the hole differ from the real ones. This can affect the atomization of the spray.

In the case of this nominal geometry, the first 3 millimeters downstream of the nozzle exit show that the core of the spray remains intact until the area closest to the outlet boundary where it seems to start atomizing, corresponding to the so-called primary atomization. This indicates that due to the effect of the shape of the counterbore geometry, the instabilities grow more slowly. The representation of the velocity together with the isosurfaces of the Q-criterion reflects how the drop in velocity coincides with the zones that are further away from the spray's core, which means the mixture of the liquid with the ambient gas and the beginning of the formation of structures that lead to the atomization of the spray. Vortices start to be generated at the entrance of the holes due to the deviation of the flow. These remain and continue to develop in the internal region, probably causing the formation of

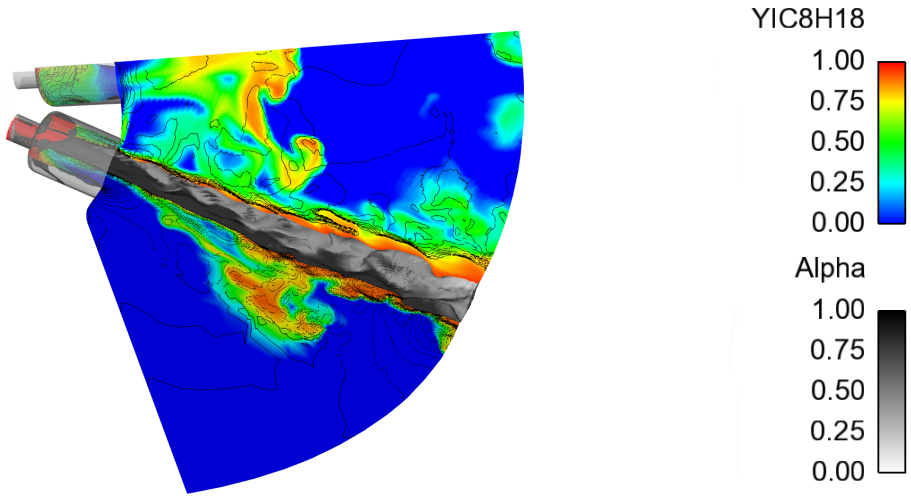

(a) Iso-surface of alpha joined to liquid mass fraction contours and velocity lines.

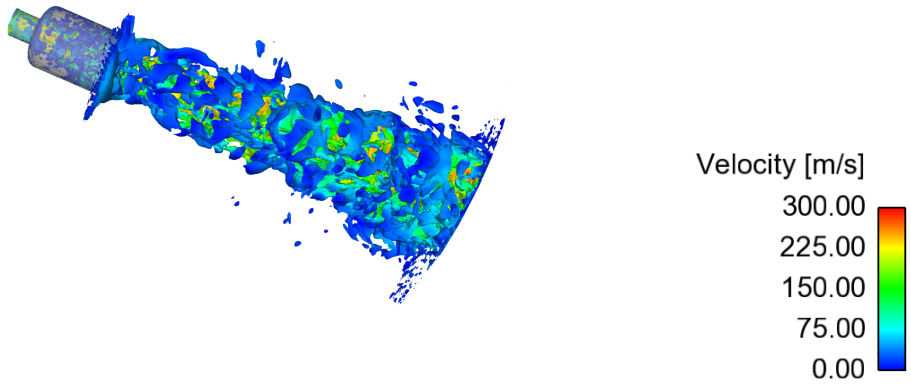

(b) Spray and vortex structures shown by the iso-surface of Q-criterion = -1E11 s^{-2} colored by velocity variable.

Figure 9: Close look at the near-nozzle region of the spray and vortex structures. Time = 100 µs aSOI.

unstable structures and ligaments that later result in a primary atomization. This correlation effect between vortex structures and primary rupture was observed by Shi et al. (2017) and Yue et al. (2020), who report evidence of a vortex-driven primary breakup mechanism in diesel and gasoline injectors,

respectively.

As part of the analysis of the stationary phase of the simulation, which corresponds to the moment when the needle is at its maximum opening, the liquid mass fraction has been averaged and compared with the root-mean-square (RMS) velocity. As mentioned above, one of the main characteristics of LES models is the ability to solve large turbulent scales. The root-mean-square velocity is directly related with the turbulence intensity and is the greatest indicator of the resolved energy in the domain. The resolved part of the energy is commonly represented from the turbulent kinetic energy (TKE). The turbulent kinetic energy is deduced from the filtered velocity fluctuations $\tilde{u}'_{rms}$, expressed by the use of the resolved instantaneous velocity vector $\tilde{u}$ and its time-averaged value noted $< \tilde{u} >$: $\tilde{u}'_{rms} = \sqrt{< \tilde{u}\tilde{u} > - < \tilde{u} >^2}$ then $k_{res} = \frac{1}{2}\tilde{u}'_{rms}\tilde{u}'_{rms}$. Figure 10 represents the time-averaged liquid mass fraction and the iso-surfaces corresponding to the $\tilde{u}'_{rms}$ in a cut-plane along holes 3-7. The central part of the spray near the nozzle outlet remains intact and therefore there are no signs of $\tilde{u}'_{rms}$. As the fluid moves away from the injector outlet, it is observed how the liquid mixes with the ambient gas producing turbulent phenomena which in turn increase the mixing and atomization of the spray. It is therefore affirmed and corroborated that root-mean-square velocity ($\tilde{u}'_{rms}$) fluctuation has higher levels of spatially located velocity fluctuations in areas where the liquid-vapor mixture is noticeable.

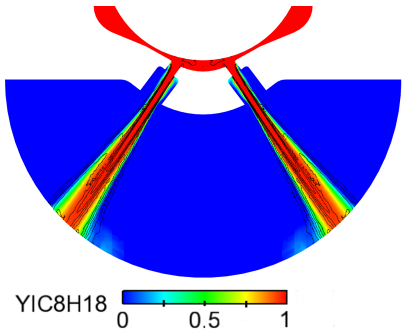

Figure 10: Vertical cut-plane representing the liquid mass fraction and the iso-surfaces corresponding to the $\tilde{u}'_{rms}$ in the LES approach.

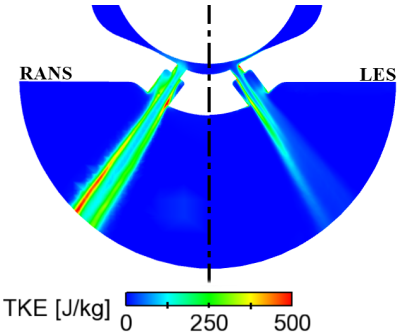

Figure 11: Modeled Turbulent Kinetic Energy (TKE) comparison between the two different approaches, RANS on the left part and LES on the right part.

Figure 11 depicts the modeled turbulent kinetic energy for the same orifice (hole 3) in both approaches, RANS on the left and LES on the right. As

mentioned above, LES models stand out for resolving much of the turbulent energy and modeling the small scales motion. In contrast, RANS models all turbulent scales. Therefore, the picture demonstrates that RANS approach has a higher modeled turbulent kinetic energy compared to LES, but when evaluating the total energy (modeled + resolved in case of LES and only modeled in RANS), it is the LES model that exhibits the highest turbulence. The quality criteria used in the previous sections (Section 2.6) proved how the mesh was sufficient for this study to provide accurate results.

Focusing on the image on the right where the TKE belonging to the LES approximation is reflected, it can be noticed how the modeled energy corresponds to the area where the spray core remains intact, without mixing with the environment. For this reason, the $\tilde{u}'_{rms}$ is very small as shown in Figure 10. As described above, the $\tilde{u}'_{rms}$ is directly related to the resolved TKE, so if the $\tilde{u}'_{rms}$ is very small, it means that in those areas the energy is not being resolved but modeled. This statement is supported by Figure 11 where it is verified that in those areas where the $\tilde{u}'_{rms}$ is low, which means that the turbulence scales are very small, the modeled TKE becomes more important.

The spray angle can be defined as the jet opening measured from nozzle tip to some distance downstream of the flow while the plume direction is the angle between the vertical injector axis and the spray axis (Figure 12). These parameters are essential aspects and determinants of the result precision when analyzing the external flow from, for example, Droplet Discrete Model (DDM) approximations. Mainly, the lack of experimental data due to the complexity of the study has meant that much of the studies known to date have been carried out starting from an *ad hoc* value of spray angle and calibrating it until the results chosen for validation coincide with the experimental ones. This is an imprecise way of carrying out these analysis, giving rise to incorrect approximations. As proved by both, previous mass flow analysis of individual orifices and studies conducted by other institutions (Baldwin et al. (2016)), the geometry influences the development of the jet. For this reason, it is important that the technique of angle calculation estimates the angles for each of the sprays in order to observe differences in the behavior, if any.

The calculation of the angles is often performed from a variable that defines the spray itself, either the velocity, the liquid volume fraction or, as in this case, the liquid mass fraction. When the liquid leaves the injector nozzle and comes into contact with the environment, it begins to mix with

the non-condensable gas. This means that the contours of the spray are not being perfectly defined, but a mixture of liquid and gas. For this reason, it is necessary to choose a threshold that determines the limits of the spray being, in this case, a mass fraction greater than 0.25 considering that below this value the liquid-gas mixture is high or the liquid has evaporated to a large extent. An upper limit (z = 0.6 mm) and a lower limit (z = 1.6 mm) have been chosen to define the sample space, avoiding the influence of the outlet (Figure 12). Once the boundaries are determined, the planes that cut the holes through the center of each hole are defined. Then, the domain is vertically discretized with 20 microns samples to obtain the limits of the spray. For each of these limits, the slope is calculated taking as a reference point the center of the inner hole as defined in the ECN angle specification. Now that all the slopes have been estimated, they are averaged to acquire the spray angle as final value. The spray direction is computed in the same way by the bisector of the spray angle in each point, and averaging them at the end.

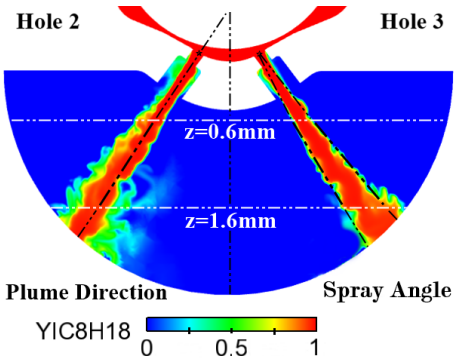

Figure 12: Definition of the spray angle and the plume direction through the time-averaged liquid mass fraction.

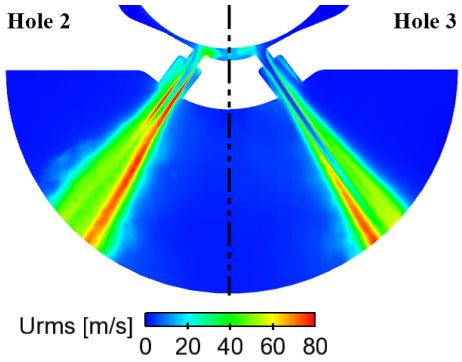

Figure 13: $\tilde{u}'_{rms}$ comparison in a vertical cut-plane along hole 2 (left) and hole 3 (right).

Figure 14 provides the results obtained from the calculation of the spray angle and plume direction for both approaches, RANS (Figure 14a) and LES (Figure 14b). Both studies, LES and RANS, show the same trend in the spray angle and plume direction evolution. There is no data in the first millisecond due to the distance taken for the angle calculation, for those first times, the jet has not developed enough to enter the acquisition window. With respect to the spray angle in both approaches, it is observed that in the first instants when the needle starts to rise and the jet begins to develop,

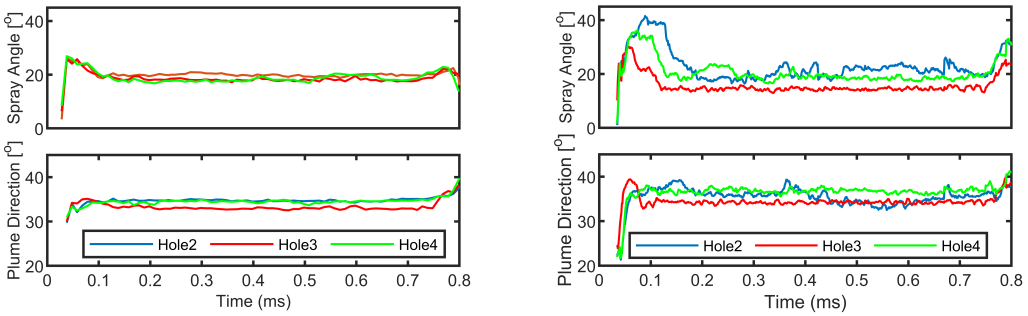

(a) RANS (b) LES

Figure 14: Spray angle and plume direction comparison between RANS (left) and LES (right) simulations for Spray G condition.

the angle of the spray is much greater (Figure 15a). Subsequently, it stabilizes corresponding to the time when the needle is at its maximum (Figures 15b and 15c). Finally, at the closing stage, it is observed how the angle tends to open again (Figure 15d). This phenomenon is predominantly due to the fact that the environment where the fuel is being injected is quiescent prior to injection, putting up resistance to the incoming fluid and therefore increasing the spray angle. In addition, in the first instants of the injection, the liquid tends to occupy the entire volume of the orifice and the counter-bore which can also cause the spray angle to be larger initially. This effect is mitigated as the needle rises and the injection develops by the existing recirculation of the non-condensable gas into the counter-bore. It is important to mention that this effect of increasing the spray opening angle at the beginning of the injection and at the end of the injection is common and widely reported in the literature (Taşkiran and Ergeneman (2011), Payri et al. (2017)).

The RANS results indicate a steady behavior of the angle without oscillations in time and with similar results between sprays. On the contrary, in LES, both spray angle and plume direction have higher variability which is reflected in the standard deviation reported in Table 4 and that can be caused by the generation of vortices along the jet. In addition, the LES results reveal that for orifices 2 and 4 the spray angle is similar while the results for hole 3 are lower. On the one hand, the orientation of the mesh, since hole 3 is oriented with the cartesian mesh, could influence the results as seen in other works (Saha et al. (2016b)). On the other hand, the studied

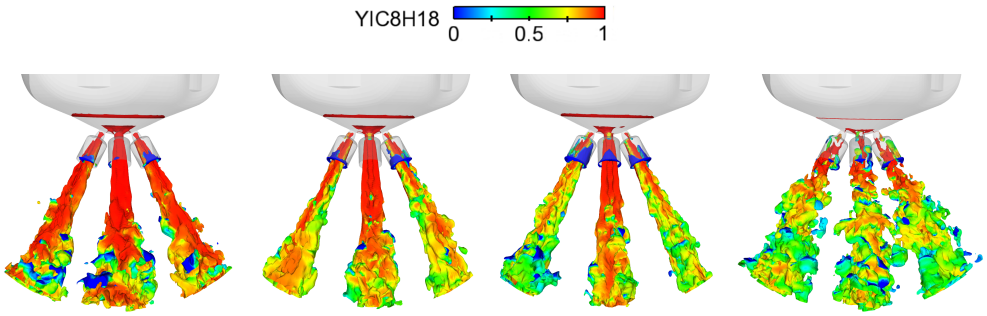

(a) t = 0.075 ms (b) t = 0.125 ms (c) t = 0.675 ms (d) t = 0.775 ms

Figure 15: Iso-surface of velocity variable colored by liquid mass fraction for different time steps corresponding to two opening times and two closing times.

geometry has 5 bumps and 8 orifices, so the flow distribution is not the same in all of them. Therefore, the turbulence generated upstream of the injector may affect some directions more than others, being this effect more visible in the LES approaches. To support this statement, the velocity streamlines have been presented in Figure 16, which have as their origin the plane that cuts the inner holes. It can be noticed how the streamlines are not equally distributed along the three holes, which has consequences at the exit of the orifice and thus the angle of the jet is affected. Furthermore, the velocity of the streamlines at the nozzle exit is also different between the three holes, which changes the diffusion of the momentum with the surrounding ambient air and can make these differences even greater. In addition to this, the difference between orifices can also be seen in the direction of the spray. Thus, orifice 3 is deflected inwards, deviating from the geometrical axis of the orifice, while the other orifices show a minimal deviation. This deflection effect is displayed in Figure 12, where the counter-bore of orifice 2 (on the left) is practically full of liquid while orifice 3 (on the right) is largely occupied by non-condensable gas. This recirculation of air is the main reason of the deflection of the spray, causing it to deviate from the geometric axis of the orifice.

The time-averaged and standard deviation spray angle and plume direction for both approaches studied are displayed in Table 4 and compared with the literature results (Payri et al. (2019), Manin et al. (2015)). The LES results state a narrower spray in hole 3 while holes 2 and 4 are around 20°. With respect to the plume direction, a small deviation of approximately

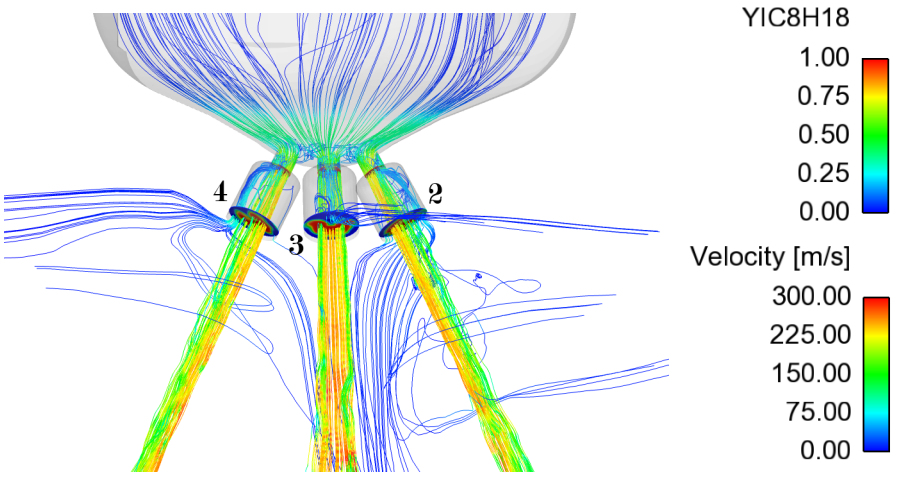

Figure 16: Velocity streamlines starting at the small orifice planes which are colored with the mass fraction of liquid. Time = 150 µs aSOI.

Table 4: Time-averaged measurements and standard deviation for the spray angle and plume direction in RANS and LES simulations.

	LES		RANS	
	Spray Angle [°]	Plume Direction [°]	Spray Angle [°]	Plume Direction [°]
Hole 2	20.03 ± 2.21	36.04 ± 1.23	19.98 ± 0.41	34.73 ± 0.14
Hole 3	14.41 ± 0.52	34.21 ± 0.28	18.16 ± 0.45	32.97 ± 0.24
Hole 4	19.56 ± 1.73	36.88 ± 0.46	17.78 ± 0.51	34.46 ± 0.28
Lit. results	Spray angle [°] ≈ 20 [Payri et al. (2019)]		Plume Direction [°] ≈ 34 [Manin et al. (2015)]	

1-1.5° is observed in holes 2 and 4 while hole 3, in both approaches, has more significant deviation. The reasons for these results have been explained above. In the case of LES, if the spray amplitude is related to the $\tilde{u}'_{rms}$ as shown in Figure 13, it can be seen that those orifices with a larger spray angle are also those with a higher $\tilde{u}'_{rms}$ at the top of the jet and along the length of the jet. In these areas of higher $\tilde{u}'_{rms}$, the liquid-vapor mixture is greater, which lead to a larger spray opening. In the case of RANS, the spray angle and plume direction resemble results previously published in the literature. The deviation of the spray angle from the geometric axis of the orifice can be highlighted. The plume direction is smaller compared to the LES model, a result that could be intuited from the calculated area C_a in Table 3. The

area coefficient in the case of RANS was lower than the experimental one and than the one obtained with LES, thus suggesting the presence of a greater gas recirculation inside the orifices, generating the deflection of the jet. In conclusion, predicted trends from both approaches estimate the liquid plume direction and spray angle close to literature values and contribute to the GDi spray behavior understanding.

4. Conclusions

The current research carried out a numerical study of the internal and near-nozzle flow for a multi-hole GDi injector, in particular the Spray G injector from ECN. LES approach is selected for the turbulence modeling of the transient and steady phases of the injection event. The main findings of this report are summarized below,

- As the results were compared with RANS data, a sample study has been carried out to ensure precision in the comparison. The analysis reveals that 3 simulations are sufficient to accurately carry out the above-mentioned comparison. It is worth mentioning that if the study is focused on macroscopic variables such as ROI or ROM, a single simulation is adequate for the analysis as the standard deviation between simulations is small.

- Concerning the mass flow rate and momentum flux results, the quasi-steady condition is achieved before the needle lift reaches its maximum. Comparison of the results obtained with the LES model with the experimental data reveals differences of 9% in the ROI results and 6% in the ROM values. This is mainly due to the fact that the applied symmetry condition does not correctly capture the fluid behavior. In combination to this effect, the data acquisition distance can influence the momentum flux results.

- The calculation of dimensionless nozzle flow coefficients reflects the same conclusions as the ROI and ROM profiles. The discharge coefficient of this type of injectors is low due to the existence of the recirculation phenomenon which reduces the presence of liquid inside the counter-bore. The mentioned differences in ROI and ROM translate into higher discharge, momentum and area coefficient compared to the experimental results. LES models underestimate the flow detachment

occurring inside the orifice while the RANS approach has an inverse behavior, overestimating this effect.

- The use of LES approaches has allowed a more accurate study of spray behavior, improving the modeling of primary atomization by aerodynamic interaction. During the needle opening phase there is a strong interaction between jets, so it is necessary to have the adjacent jets available for the study of the atomization process. In the steady part of the simulation, high $\tilde{u}'_{rms}$ fluctuation values have been observed in areas where the liquid-vapor mixture is noteworthy. These same areas where $\tilde{u}'_{rms}$ is high have very low values of modeled TKE. Therefore, the modeled TKE becomes important in areas where the spray remains intact without interaction with the environment.

- Referring to the spray angle and plume direction, results have been shown as a function of time, something that, to the author's best knowledge, has not been studied to date. The results obtained from RANS model do not present variation between sprays and are steady over time, without oscillations. On the contrary, LES approach displays higher variability with time and between orifices. This is caused by the asymmetric effect of upstream turbulence due to the distribution of bumps and holes in the geometry, which is enhanced in LES models. Predicted trends from both turbulence models estimates values of spray angle and liquid plume direction close to the literature.

As future works, applying the presented methodology to the analysis of the transient (opening and closing) and steady phases of the injection using different sub-grid models for the turbulence could give interesting results. On the other hand, the calculation of the angle as a function of time could be used for coupling Eulerian-Lagrangian approximations, giving more accurate results of the spray behavior.

Acknowledgments

This research was funded by Generalitat Valenciana through project reference AICO/2020/208 titled "Nuevos conceptos en inyección de gasolina (NCIG)". Additionally, authors would like to thank the "Fundación del Centro de Supercomputación de Castilla y León" (FCSCL) and "ACT now HPC Cloud Cluster" for allowing the use of their clusters to perform part of the

simulations carried out in this work. Also to Abian Bautista and Javier Varea for their help in the analysis. Finally mention that the Ph.D. student María Martínez has been funded by a grant from the Government of Generalitat Valenciana with reference ACIF/2018/118 and financial support from The European Union.

References

[1] Agarwal, A., Trujillo, M.F., 2020. The effect of nozzle internal flow on spray atomization. International Journal of Engine Research 21, 55–72. doi:10.1177/1468087419875843.

[2] Baldwin, E., Grover, R., Parrish, S.E., Duke, D.J., Matusik, K.E., Powell, C.F., Kastengren, A.L., Schmidt, D.P., 2016. String flash-boiling in gasoline direct injection simulations with transient needle motion. International Journal of Multiphase Flow 87, 90–101. doi:10.1016/j.ijmultiphaseflow.2016.09.004.

[3] Battistoni, M., Duke, D.J., Swantek, A.B., Tilocco, F.Z., Powell, C.F., Som, S., 2015. Effects of noncondensable gas on cavitating nozzles. Atomization and Sprays 25, 453–483. doi:10.1615/AtomizSpr.2015011076.

[4] Battistoni, M., Som, S., Longman, D.E., 2014. Comparison of mixture and multifluid models for in-nozzle cavitation prediction. Journal of Engineering for Gas Turbines and Power 136. doi:10.1115/1.4026369.

[5] Bilicki, Z., Kestin, J., 1990. Physical Aspects of the Relaxation Model in Two-Phase Flow. Proceedings of the Royal Society A: Mathematical, Physical and Engineering Sciences 428, 379–397. doi:10.1098/rspa.1990.0040.

[6] Celik, I., Klein, M., Janicka, J., 2009. Assessment measures for engineering LES applications. Journal of Fluids Engineering, Transactions of the ASME 131, 0311021–03110210. doi:10.1115/1.3059703.

[7] Celik, I.B., Cehreli, Z.N., Yavuz, I., 2005. Index of resolution quality for large eddy simulations. Journal of Fluids Engineering, Transactions of the ASME 127, 949–958. doi:10.1115/1.1990201.

[8] Cheng, Q., Xu, M., Zhang, Z., Xie, N., 2017. Investigation on the spray characteristics of standard gasoline, n-pentane, iso-octane and ethnaol with a novel heated tip SIDI injector. Applied Thermal Engineering 110, 539–552. doi:10.1016/j.applthermaleng.2016.07.201.

[9] Cordier, M., Itani, L., Bruneaux, G., 2020. Quantitative measurements of preferential evaporation effects of multicomponent gasoline fuel sprays at ECN Spray G conditions. International Journal of Engine Research 21, 185–198. doi:10.1177/1468087419838391.

[10] Desantes, J.M., Payri, R., Salvador, F.J., Gimeno, J., 2003. Measurements of spray momentum for the study of cavitation in diesel injection nozzles. SAE Technical Paper 2003-01-0703 doi:10.4271/2003-01-0703.

[11] Duke, D.J., Kastengren, A.L., Matusik, K.E., Swantek, A.B., Powell, C.F., Payri, R., Vaquerizo, D., Itani, L., Bruneaux, G., Grover, R.O., Parrish, S., Markle, L., Schmidt, D., Manin, J., Skeen, S.A., Pickett, L.M., 2017. Internal and near nozzle measurements of Engine Combustion Network "Spray G" gasoline direct injectors. Experimental Thermal and Fluid Science 88, 608–621. doi:10.1016/j.expthermflusci.2017.07.015.

[12] Duke, D.J., Swantek, A.B., Sovis, N.M., Tilocco, F.Z., Powell, C.F., Kastengren, A.L., Gürsoy, D., Biçer, T., 2015. Time-resolved X-ray Tomography of Gasoline Direct Injection Sprays. SAE International Journal of Engines 9, 143–153. doi:10.4271/2015-01-1873.

[13] Dymond, J.H., Glen, N.F., Isdale, J.D., 1985. Transport properties of nonelectrolyte liquid mixtures-VII. Viscosity coefficients for isooctane and for equimolar mixtures of isooctane + n-octane and isooctane + n-dodecane from 25 to 100^{o}C at pressures up to 500 MPa or to the freezing pressure. International Journal of Thermophysics doi:10.1007/BF00522146.

[14] Ferziger, J., Peric, M., 2002. Computational Methods for Fluid Dynamics. Berlin: Spinger.

[15] Fukagata, K., Zahrai, S., Bark, F.H., 1998. Force balance in a turbulent particulate channel flow. International Journal of Multiphase Flow 24, 867–887. doi:10.1016/S0301-9322(98)00014-7.

[16] Geurts, B.J., Fröhlich, J., 2002. A framework for predicting accuracy limitations in large-eddy simulation. Physics of Fluids 14. doi:10.1063/1.1480830.

[17] Grover, R.O., Duke, D.J., Matusik, K.E., Kastengren, A.L., 2016. String Flash-Boiling in Flashing and Non-Flashing Gasoline Direction Injection Simulations with Transient Needle Motion University of Massachusetts Amherst General Motors Research and Development Energy Systems Division , Argonne National Laboratory , Lem. ILASS Americas 28th Annual Conference on Liquid Atomization and Spray Systems .

[18] Guo, H., Nocivelli, L., Torelli, R., Som, S., 2020. Towards understanding the development and characteristics of under-expanded flash boiling jets. International Journal of Multiphase Flow 129, 103315. doi:10.1016/j.ijmultiphaseflow.2020.103315.

[19] Keskinen, J.P., Vuorinen, V., Kaario, O., Larmi, M., 2016. Influence of mesh deformation on the quality of large eddy simulations. International Journal for Numerical Methods in Fluids doi:10.1002/fld.4215.

[20] Lee, S., Park, S., 2014. Spray atomization characteristics of a GDI injector equipped with a group-hole nozzle. Fuel 137, 50–59. doi:10.1016/j.fuel.2014.07.063.

[21] Li, Y., Guo, H., Zhou, Z., Zhang, Z., Ma, X., Chen, L., 2019. Spray morphology transformation of propane, n-hexane and iso-octane under flash-boiling conditions. Fuel 236, 677–685. doi:10.1016/j.fuel.2018.08.160.

[22] Manin, J., Jung, Y., Skeen, S.A., Pickett, L.M., Parrish, S.E., Markle, L., 2015. Experimental Characterization of DI Gasoline Injection Processes. SAE Technical Paper 2015-01-1894 doi:10.4271/2015-01-1894.

[23] Matusik, K.E., Duke, D.J., Sovis, N., Swantek, A.B., Powell, C.F., Payri, R., Vaquerizo, D., Giraldo-Valderrama, S., Kastengren, A.L., 2017. A study on the relationship between internal nozzle geometry and injected mass distribution of eight ECN Spray G nozzles., in: ILASS2017 - 28th European Conference on Liquid Atomization and Spray Systems, pp. 6–8. doi:10.4995/ilass2017.2017.4766.

[24] Medina, M., Alzahrani, F.M., Fatouraie, M., Wooldridge, M.S., 2020. Mechanisms of fuel injector tip wetting and tip drying based on experimental measurements of engine-out particulate emissions from gasoline direct-injection engines. International Journal of Engine Research doi:10.1177/1468087420916052.

[25] Menon, S., Yeung, P.K., Kim, W.W., 1996. Effect of subgrid models on the computed interscale energy transfer in isotropic turbulence. Computers and Fluids 25, 165–180. doi:10.1016/0045-7930(95)00036-4.

[26] Meyers, J., Geurts, B.J., Baelmans, M., 2003. Database analysis of errors in large-eddy simulation. Physics of Fluids 15, 2740–2755. doi:10.1063/1.1597683.

[27] Mohan, B., Badra, J., Sim, J., Im, H.G., 2020. Coupled in-nozzle flow and spray simulation of Engine Combustion Network Spray-G injector. International Journal of Engine Research doi:10.1177/1468087420960612.

[28] Mohapatra, C.K., Schmidt, D.P., Sforozo, B.A., Matusik, K.E., Yue, Z., Powell, C.F., Som, S., Mohan, B., Im, H.G., Badra, J., Bode, M., 2020. Collaborative investigation of the internal flow and near-nozzle flow of an eight-hole gasoline injector (Engine Combustion Network Spray G). International Journal of Engine Research doi:10.1177/1468087420918449.

[29] Moulai, M., Grover, R., Parrish, S., Schmidt, D., 2015. Internal and Near-Nozzle Flow in a Multi-Hole Gasoline Injector Under Flashing and Non-Flashing Conditions. SAE Technical Paper doi:10.4271/2015-01-0944.

[30] Navarro-Martinez, S., Tretola, G., Yosri, M.R., Gordon, R.L., Vogiatzaki, K., 2020. An investigation on the impact of small-scale models in gasoline direct injection sprays (ECN Spray G). International Journal of Engine Research 21, 217–225. doi:10.1177/1468087419889449.

[31] Pandal, A., Garcia-Oliver, J.M., Pastor, J.M., 2020. Eulerian CFD modeling of nozzle geometry effects on ECN Sprays A and D: assessment and analysis. International Journal of Engine Research 21, 73–88. doi:10.1177/1468087419882500.

[32] Payri, R., Gimeno, J., Marti-aldaravi, P., Martínez, M., 2019. Nozzle Flow Simulation of GDi for Measuring Near-Field Spray Angle and Plume Direction. SAE Technical Paper 2019-01-0280 , 1–11doi:10.4271/2019-01-0280.Abstract.

[33] Payri, R., Gimeno, J., Martí-aldaraví, P., Martínez, M., 2021. Large Eddy Simulations of the fuel injection and mixing process of the ECN GDi Injector Spray G. 15thTriennial International Conference on Liquid Atomization and Spray Systems , 1–8doi:10.2218/iclass.2021.5874.

[34] Payri, R., Gimeno, J., Martí-Aldaraví, P., Vaquerizo, D., 2015. Momentum Flux Measurements on an ECN GDi Injector, in: SAE Technical Paper 2015-01-1893. doi:10.4271/2015-01-1893.

[35] Payri, R., Gimeno, J., Martí-Aldaraví, P., Vaquerizo, D., 2016. Internal flow characterization on an ECN GDi injector. Atomization and Sprays 26, 889–919. doi:10.1615/AtomizSpr.2015013930.

[36] Payri, R., Guardiola, C., Salvador, F.J., Gimeno, J., 2004. Critical cavitation number determination in Diesel injection nozzles. Experimental Techniques 28, 49–52. doi:10.1111/j.1747-1567.2004.tb00164.x.

[37] Payri, R., Salvador, F.J., Martí-Aldaraví, P., Vaquerizo, D., 2017. ECN Spray G external spray visualization and spray collapse description through penetration and morphology analysis. Applied Thermal Engineering 112, 304–316. doi:10.1016/j.applthermaleng.2016.10.023.

[38] Pickett, L., Bruneaux, G., Payri, R., 2020. Engine combustion network special issue. International Journal of Engine Research 21, 11–14. doi:10.1177/1468087419882247.

[39] Pope, S., 2009. Turbulent Flows. sixth ed., Cambridge University Press.

[40] Raza, M., Chen, L., Leach, F., Ding, S., 2018. A Review of particulate number (PN) emissions from gasoline direct injection (gdi) engines and their control techniques. Energies 11. doi:10.3390/en11061417.

[41] Rhie, C.M., Chow, W.L., 1983. Numerical study of the turbulent flow past an airfoil with trailing edge separation. AIAA Journal 21, 1525–1532. doi:10.2514/3.8284.

[42] Richards, K.J., Senecal, P.K., Pomraning, E., 2018. Convergent Science v2.4 Documentation. Convergent Science Inc. , 1207.

[43] Saha, K., Som, S., Battistoni, M., 2016a. Parametric Study of HRM for Gasoline Sprays. ILASS Americas 28th Annual Conference on Liquid Atomization and Spray Systems, Dearborn, MI, May 2016 .

[44] Saha, K., Som, S., Battistoni, M., Li, Y., Pomraning, E., Senecal, P.K., 2016b. Numerical Investigation of Two-Phase Flow Evolution of In- and Near-Nozzle Regions of a Gasoline Direct Injection Engine During Needle Transients. SAE International Journal of Engines 9, 2016–01–0870. doi:10.4271/2016-01-0870.

[45] Schmidt, D.P., Corradini, M.L., Rutland, C.J., 1999. A two-dimensional, non-equilibrium model of flashing nozzle flow, in: 3rd ASME/JSME Joint Fluids Engineering Conference.

[46] Schmidt, D.P., Gopalakrishnan, S., Jasak, H., 2010. Multi-dimensional simulation of thermal non-equilibrium channel flow. International Journal of Multiphase Flow 36, 284–292. doi:10.1016/j.ijmultiphaseflow.2009.11.012.

[47] Shahangian, N., Sharifian, L., Uehara, K., Noguchi, Y., Martinez, M., Marti-aldaravi, P., Payri, R., 2020. Transient nozzle flow simulations of gasoline direct fuel injectors. Applied Thermal Engineering , 115356doi:10.1016/j.applthermaleng.2020.115356.

[48] Shi, J., Aguado Lopez, P., Gomez Santos, E., Guerrassi, N., Dober, G., Bauer, W., Lai, M.C., Wang, J., 2017. Evidence of vortex driven primary breakup in high pressure fuel injection, in: ILASS2017 - 28th European Conference on Liquid Atomization and Spray Systems, pp. 6–8. doi:10.4995/ilass2017.2017.5707.

[49] Shi, J., Gomez Santos, E., Hoffmann, G., Dober, G., 2018. Large Eddy Simulation as an Effective Tool for GDI Nozzle Development. MTZ worldwide 79, 58–63. doi:10.1007/s38313-018-0089-2.

[50] Taşkiran, Ö.O., Ergeneman, M., 2011. Experimental study on diesel spray characteristics and autoignition process. Journal of Combustion 2011. doi:10.1155/2011/528126.

[51] Torregrosa, A.J., Payri, R., Javier Salvador, F., Crialesi-Esposito, M., 2020. Study of turbulence in atomizing liquid jets. International Journal of Multiphase Flow 129, 103328. doi:10.1016/j.ijmultiphaseflow.2020.103328.

[52] Xue, Q., Battistoni, M., Som, S., Quan, S., Senecal, P.K., Pomraning, E., Schmidt, D., 2014. Eulerian CFD Modeling of Coupled Nozzle Flow and Spray with Validation Against X-Ray Radiography Data. SAE International Journal of Engines 7, 2014–01–1425. doi:10.4271/2014-01-1425.

[53] Yoshizawa, A., Horiuti, K., 1985. A Statistically-Derived Subgrid-Scale Kinetic Energy Model for the Large-Eddy Simulation of Turbulent Flows. Journal of the Physical Society of Japan 54, 2834–2839. doi:10.1143/JPSJ.54.2834.

[54] Yue, Z., Battistoni, M., Som, S., 2020. Spray characterization for engine combustion network Spray G injector using high-fidelity simulation with detailed injector geometry. International Journal of Engine Research 21, 226–238. doi:10.1177/1468087419872398.

[55] Zamani, H., Hosseini, V., Afshin, H., Allocca, L., Baloo, M., 2016. Large eddy simulation of GDI single-hole and multi-hole injector sprays with comparison of numerical break-up models and coefficients. Journal of Applied Fluid Mechanics 9, 1013–1022. doi:10.18869/acadpub.jafm.68.225.22889.

[56] Zhao, H., 2010. Overview of gasoline direct injection engines. Di, Woodhead Publishing Limited. doi:10.1533/9781845697327.1.

[57] Zhao, H., Quan, S., Dai, M., Pomraning, E., Senecal, P.K., Xue, Q., Battistoni, M., Som, S., 2014. Validation of a Three-Dimensional Internal Nozzle Flow Model Including Automatic Mesh Generation and Cavitation Effects. Journal of Engineering for Gas Turbines and Power 136. doi:10.1115/1.4027193.